Anthropogenic aerosols offsetting ocean warming less efficiently since the 1980s

AGU ADVANCING EARTH AND SPACE SCIENCES

Geophysical Research Letters®

RESEARCH LETTER
10.1029/2023GL105374

Anthropogenic Aerosols Offsetting Ocean Warming Less Efficiently Since the 1980s

Taimoor Sohail[1,2], Damien B. Irving[3], Jan D. Zika[1,2,4], and Jonathan M. Gregory[5,6]

[1]School of Mathematics and Statistics, University of New South Wales, Sydney, NSW, Australia, [2]Australian Center for Excellence in Antarctic Science, University of New South Wales, Sydney, NSW, Australia, [3]Commonwealth Scientific and Industrial Research Organisation (CSIRO), Hobart, TAS, Australia, [4]UNSW Data Science Hub (uDASH), University of New South Wales, Sydney, NSW, Australia, [5]National Centre for Atmospheric Science, University of Reading, Reading, UK, [6]Met Office Hadley Centre, Exeter, UK

Key Points:

- Since 1980, aerosol-driven ocean cooling has decelerated substantially, alongside a drop in ocean heat uptake efficiency
- The drop in ocean heat uptake efficiency is limited to the tropics, which may have equilibrated to ongoing aerosol-driven radiative forcing
- Air-sea fluxes into the coldest fraction of the ocean continue to offset greenhouse gas-driven ocean warming

Supporting Information:

Supporting Information may be found in the online version of this article.

Correspondence to:

T. Sohail,
t.sohail@unsw.edu.au

Citation:

Sohail, T., Irving, D. B., Zika, J. D., & Gregory, J. M. (2023). Anthropogenic aerosols offsetting ocean warming less efficiently since the 1980s. *Geophysical Research Letters*, *50*, e2023GL105374. https://doi.org/10.1029/2023GL105374

Received 12 JUL 2023
Accepted 16 NOV 2023

Abstract Greenhouse gases and aerosols play a major role in controlling global climate change. Greenhouse gases drive a radiative imbalance which warms the ocean, while aerosols cool the ocean. Since 1980, the effective radiation felt by the planet due to anthropogenic aerosols has leveled off, global ocean cooling due to aerosols has decelerated, and greenhouse gas-driven ocean warming has accelerated. We explore the deceleration of aerosol-driven ocean cooling by quantifying a time- and spatially varying ocean heat uptake efficiency, defined as the change in the rate of global ocean heat storage per degree of cooling surface temperature. In aerosol-only simulations, ocean heat uptake efficiency has decreased by 43 ± 14% since 1980. The tropics and sub-tropics have driven this decrease, while the coldest fraction of the ocean continues to sustain cooling and high ocean heat uptake efficiency. Our results identify a growing trend toward less efficient ocean cooling due to aerosols.

Plain Language Summary The composition of the atmosphere has a major impact on our climate. Greenhouse gases warm the planet, while aerosols (i.e., suspensions of particles in the atmosphere) cool the planet, and most of this change is absorbed by the oceans. Since 1980, the rate of cooling of the planet due to aerosols has plateaued. In the past few decades, the ocean has begun to equilibrate to this change, and this work explores where and when this equilibration has occurred in the ocean based on global climate models. To understand this change, we use an "ocean heat uptake efficiency" metric which describes how much additional heat builds up in the ocean for a given degree of surface temperature gain (or loss). We find that the ocean is cooling more slowly given a degree of surface cooling due to aerosols compared to the pre-1980s. This change is largely driven by the tropics and sub-tropics, where the ocean has stopped cooling in response to aerosol-driven negative surface temperatures. Polar and sub-polar regions, however, continue to cool due to aerosols. These changes are occurring alongside accelerating greenhouse gas-driven warming, suggesting that the relative role of aerosols in cooling our climate is weakening.

1. Introduction

Variations in the composition of the earth's atmosphere, namely, changing concentrations of Greenhouse gases (GHGs), aerosols and ozone, cause anthropogenic climate change. GHGs primarily inhibit loss of heat to space, and thus warm the climate system. The ocean absorbs a large proportion of the heat that consequently accumulates. A recent estimate suggests that approximately 89% of the excess heat in the climate system has been absorbed by the global oceans since 1970 (Schuckmann et al., 2020). Anthropogenic aerosols (AAs) cool the climate system (Gleckler et al., 2006; Ramanathan et al., 2001), and thus offset some of the GHG-driven ocean warming. They also introduce spatial heterogeneity into the ocean warming pattern (Delworth et al., 2005; Irving et al., 2019).

In order to understand the effect of GHGs and AAs on the ocean and climate, single-forcing simulations have been conducted by the Detection and Attribution Model Intercomparison Project (DAMIP) (Gillett et al., 2016), which is part of the Coupled Model Intercomparison Project (Phase 6; CMIP6; Eyring et al. (2016)). In DAMIP, coupled atmosphere–ocean three-dimensional climate models are integrated from 1850 to 2014 in separate experiments forced by historical atmospheric concentrations of anthropogenic GHGs (*GHG-only*), aerosols (*AA-only*) and natural forcings (volcanic aerosol and variability in solar irradiance) individually, to compare their impact on

the climate system (Gillett et al., 2016). The single-forcing simulations are compared with the standard CMIP6 historical experiment which includes all forcings together. Past research with DAMIP simulations has shown that GHG-driven ocean warming has been offset by aerosols across a range of depths in an ensemble of climate models (Bilbao et al., 2019). This offsetting effect is stronger in the Northern Hemisphere than the Southern Hemisphere due to uneven aerosol concentrations in the atmosphere (Irving et al., 2019).

Since 1980, however, the aerosol-driven change in top-of-atmosphere net downward radiative flux, or effective radiative forcing (ERF), has leveled off at approximately -1 W/m^2 relative to the pre-industrial climate (allowing for atmospheric adjustments) (Smith et al., 2021). In contrast, the GHG-driven ERF has continued to grow, reaching over 2 W/m^2 (relative to the pre-industrial climate) by 2014 (Smith & Forster, 2021). As a result of this ERF stabilization, ocean cooling due to aerosols has plateaued in the top 2,000 m of the ocean, while GHG-driven warming has continued to accelerate (Lyu et al., 2021). Assuming this trend continues in the future, Lyu et al. (2021) produced future projections of top-2,000 m ocean heat content that are purely GHG-driven. However, the deep ocean adjusts to atmospheric changes on relatively long timescales, so the impact of the leveling off of aerosol-driven ERF on the *global* ocean heat uptake (i.e., including the portion of the ocean deeper than 2000 m) remains unclear. In general, it is unclear which regions of the ocean have equilibrated to the approximately constant aerosol ERF since 1980.

Changes in ocean heat content due to GHGs and aerosols may be expressed in terms of the "ocean heat uptake efficiency" (in W m^{-2} K^{-1}), defined as the change in the rate of storage of heat by the global ocean per degree of change in the global-mean surface temperature (e.g., Raper et al. (2002), Kuhlbrodt and Gregory (2012)). For a given model, this diagnostic is a single number which measures the response of the physical mechanisms driving ocean heat uptake in that model. Typically, ocean heat uptake efficiency has been quantified in strongly forced (i.e., 1% CO_2 or abrupt-4 $\times$ CO_2) coupled climate models (Exarchou et al., 2015; Kuhlbrodt & Gregory, 2012). Despite its utility in understanding past and future climate change, a similar estimate of ocean heat uptake efficiency has not been produced for simulated historical climate change.

In this work, we explore aerosol-driven changes to the heat content tendency budget and their constituent processes and heat uptake efficiency in a suite of CMIP6 simulations. In Section 2, we lay out the diagnostics used in the analysis, and in Section 3, we detail the models used in the study. Finally, in Section 4 we explore the temporal and spatial change in heat content and heat uptake efficiency, followed by a discussion and summary of the results in Section 5.

2. Theory

2.1. Global Diagnostics

We begin by exploring the response of the global ocean to changing surface air temperatures and ERF since 1850. The globally integrated ocean heat content is calculated from the three-dimensional temperature field $\Theta(x, y, z, t)$:

$$\mathcal{H}(t) = \rho_0 C_p \int \Theta(x, y, z, t) d\mathcal{V}, \tag{1}$$

where $\mathcal{V}$ is the volume, ρ_0 is the density and C_p is the specific heat capacity of seawater.

The ERF is sourced directly from Smith and Forster (2021) (see their Figure 1d and 1h for equivalent plots for GHG-only and AA-only runs, respectively) using a subset of the same models and ensemble members used throughout this study. Smith and Forster (2021) calculate ERF by applying the linearized energy balance equation for the Earth to a broad suite of CMIP5 and CMIP6 models: $\Delta F = \Delta N_{TOA} - \lambda \Delta T_a$, where F is the ERF, N_{TOA} is the top-of-atmosphere energy imbalance, T_a is the mean surface air temperature (relative to pre-industrial), and λ is the climate feedback parameter. We opt to source the values of ERF directly from Smith and Forster (2021) because their methodology enables us to track changes to ERF over the entire historical period.

2.2. Ocean Heat Uptake Efficiency

For timescales greater than about a year, we may assume that all of the heat storage in the earth system occurs in the ocean (Palmer & McNeall, 2014). In this case, ocean heat content tendency can be related to global-mean surface air temperature change T_a through the ocean heat uptake efficiency, as:

$$N / A_T = \kappa T_a, \tag{2}$$

where $N = \partial \mathcal{H}(t)/\partial t$ is the rate of ocean heat content change (in W), A_T is the total surface area of earth (in m^2) and κ is the ocean heat uptake efficiency (in $Wm^{-2}\,K^{-1}$). Typically, κ is conceived as a single number for a given model which captures all of the ocean heat uptake processes of the model, and does not depend on time or the nature of the forcing. However, here we do not assume that κ is a single, fixed value characteristic of a specific model, and instead, we use κ to characterize the response of model heat content to changing surface air temperature over different time periods and over different layers of the ocean. These diagnostics enable us to understand when, how and in which layers aerosols have modified the underlying temperature structure of the ocean in recent decades.

2.3. Layer-Wise Heat Content Tendency

In this work, we track changes to the ocean heat content in depth layers, as done by Bilbao et al. (2019). Ocean heat content as a function of depth (in Jm^{-1}) is calculated by horizontally integrating the global temperature field:

$$\mathcal{H}(z,t) = \rho_0 C_p \iint \Theta(x,y,z,t)\,dx\,dy, \tag{3}$$

We also investigate heat content in temperature-percentiles, following Sohail et al. (2021) and Holmes et al. (2022), to complement the depth-based analysis. Temperature-percentiles are defined in terms of the cumulatively integrated ocean volume, from hot to cold, and represent the warmest p% of the ocean by volume. The temperature $\Theta^*(p, t)$ of temperature-percentile p (between 0 and 100) is defined such that p% of the ocean volume is warmer than $\Theta^*(p, t)$, that is,

$$\int_{V_T} W(\Theta(x,y,z,t) - \Theta^*(p,t))\,dx\,dy\,dz = 0.01 p V_T, \tag{4}$$

where V_T is the total volume of the ocean, and the function $W(\delta) = 1$ for $\delta > 0$, and $W(\delta) = 0$ for $\delta \leq 0$.

Temperature-percentiles provide a complementary perspective to existing water mass-based methods of tracking property changes (e.g., at constant absolute temperature), as detailed in Sohail et al. (2021), Holmes et al. (2022), and Sohail et al. (2022). By tracking changes to the warmest p% of the ocean by volume, we:

1. Directly compare different models or observational products which may be uniformly warmer or cooler, but have the same cumulative volume distribution in percentile space.
2. Remove the effect of uniform warming or cooling over time, which would change the outcrop location of isotherms, making tracing property changes to a surface region more challenging.
3. Derive a simple heat content tendency budget where heat content tendency is a consequence of surface fluxes and mixing only (see Sohail et al. (2021) for further information).

Ocean heat content (in J) of the part of the ocean colder than percentile p is calculated as:

$$\mathcal{H}(p,t) = 0.01 V_T \rho_0 C_p \int_0^p \Theta^*(p',t)\,dp', \tag{5}$$

where p is a given temperature-percentile, V_T is the total volume of the ocean, and $\Theta^*(p, t)$ is the temperature at a given percentile. From Equation 4, the volume bounded by a temperature-percentile surface and the domain boundary is $0.01 p V_T$. To ease in the visualization of the results, we plot our results in terms of the time-mean temperature of a given percentile, $\overline{\Theta^p}$.

In temperature-percentiles, the ocean heat content tendency, $\partial \mathcal{H}(p,t)/\partial t$, is the sum of surface fluxes and mixing, $\partial \mathcal{H}(p,t)/\partial t = \mathbf{Q}(p,t) + \mathcal{M}(p,t)$. Following Sohail et al. (2021), surface air-sea heat flux tendencies, $\mathbf{Q}(p, t)$, are calculated by first area-integrating heat fluxes along a given temperature-percentile outcrop, then cumulatively integrating this quantity over time and from hot to cold percentiles, and finally computing the linear slope of this term at each temperature-percentile layer. There is no term for advection (i.e., large-scale adiabatic transport in physical space but not in Θ^* space), which does not change the distribution of volume as a function of temperature. Thus, we can diagnose the temperature-percentile layers where ocean heat content changes the most, and also the surface fluxes and mixing that contribute to this change.

3. Data

We analyze temperature and surface fluxes in nine climate models from DAMIP single-forcing experiments and their CMIP6 historical simulations. In order to limit the influence of model internal variability on ocean heat content tendency results, we take an ensemble mean across all ensemble members available for each model. For the nine models analyzed, between two and 15 ensemble members are archived, resulting in a total of 48 ensemble members. Further details of the models analyzed and their associated ensemble members are provided in Supporting Information S1 (Table S1).

We analyze the annual-averaged ocean potential temperature (*thetao*), surface air temperature (*tas*) and net downward surface heat flux (*hfds*) from 1850 to 2014 in the DAMIP and CMIP6 simulations, also using surface grid cell area (*areacella*) and ocean grid cell volume (*volcello*). Ocean heat content in temperature percentiles $\mathcal{H}(p,t)$ is calculated by volume-integrating the three-dimensional temperature field Θ as a function of temperature percentile, p (Equation 5).

Heat content tendency N is calculated for a given temperature-percentile or depth layer or for the global ocean by taking the regression slope of ocean heat content against time in decadal windows, to obtain a quantity in W (for temperature-percentiles) or Wm^{-}1 (for depth layers). The ocean heat uptake efficiency is calculated as N divided by T_a and by global surface area. In this analysis, we assume the density of sea water is $\rho_0 = 1{,}035$ kgm^{-3}, and its specific heat capacity is $C_p = 4{,}000$ J kg^{-1} K^{-1}, unless directed otherwise by modeling groups.

Following Irving et al. (2020) and Sohail et al. (2021, 2022), model drift is removed from all variables of interest by subtracting a fit as a function of time during some reference simulation, in order to exclude any effect of drift on forced trends and the global ocean heat budget. For GHG-only and AA-only DAMIP simulations, which do not include natural forcing variations, we use a cubic fit to entire pre-industrial control time series (*piControl*), which likewise has no natural forcing variation. A cubic fit is selected to ensure that centennial-scale drift is captured without overfitting onto modes of natural variability. For the CMIP6 historical simulations, a linear fit of the historical natural (*hist-nat*) simulations from the DAMIP single-forcing experiments is used, because the historical simulation *does* include historical natural forcings, and we wish to remove the long-term drift they cause, following Silvy et al. (2020). A linear fit is sufficient for this shorter (165 year) time series.

In the decades from 1995 to 2014, where the slowdown of aerosol-driven cooling is most evident, we focus on a single model (ACCESS-CM2) as an example, for which more detailed ocean heat budget tendency diagnostics are available (Bi et al., 2020). These diagnostics enable us to distinguish between the mixing mechanisms, shortwave redistribution and surface heat and volume fluxes that are driving ocean heat content change. Specifically, we diagnose the role of vertical mixing, numerical mixing, neutral diffusion, surface heat fluxes from surface volume fluxes, penetrative shortwave heating, total surface heat fluxes and other miscellaneous mixing on the ocean heat content in the AA-only and GHG-only runs of the ACCESS-CM2 model. As above, all heat content diagnostics are surface- or volume-integrated onto temperature percentiles and de-drifted from the piControl run. Tendencies are calculated from regression slopes in each percentile layer against time over the 1995 to 2014 time period. The discussion and results of this single-model analysis are presented in Figure S4 in Supporting Information S1.

To compare with model data outputs from CMIP6, we also source observational estimates of annually averaged global surface air temperature and ocean heat content from 1880 to 2014, from NASA GISSTEMPv4 (GISS, 2023; Lenssen et al., 2019) and Zanna et al. (2019), respectively. The ocean heat content data sourced from Zanna et al. (2019) is produced by combining historical sea surface temperature with a data-constrained model for subsurface temperature (using a static Green's function). Therefore, while this data does not represent "true" observed ocean heat content, it is the best available option for the long time horizon explored in this study.

4. Results

4.1. Global Ocean Heat Uptake Efficiency

We begin by exploring the global ERF, surface air temperature and ocean heat content in the AA-only, GHG-only and historical (i.e., all forcings) simulations, as well as in observations. Across all models, the GHG-only simulations exhibit a rapid acceleration in ERF, T_a and $\mathcal{H}(t)$ since 1880 (Figure 1a–1c). However, the AA-only simulations have a different ocean and ERF response. As mentioned earlier, the ERF due to aerosols has plateaued

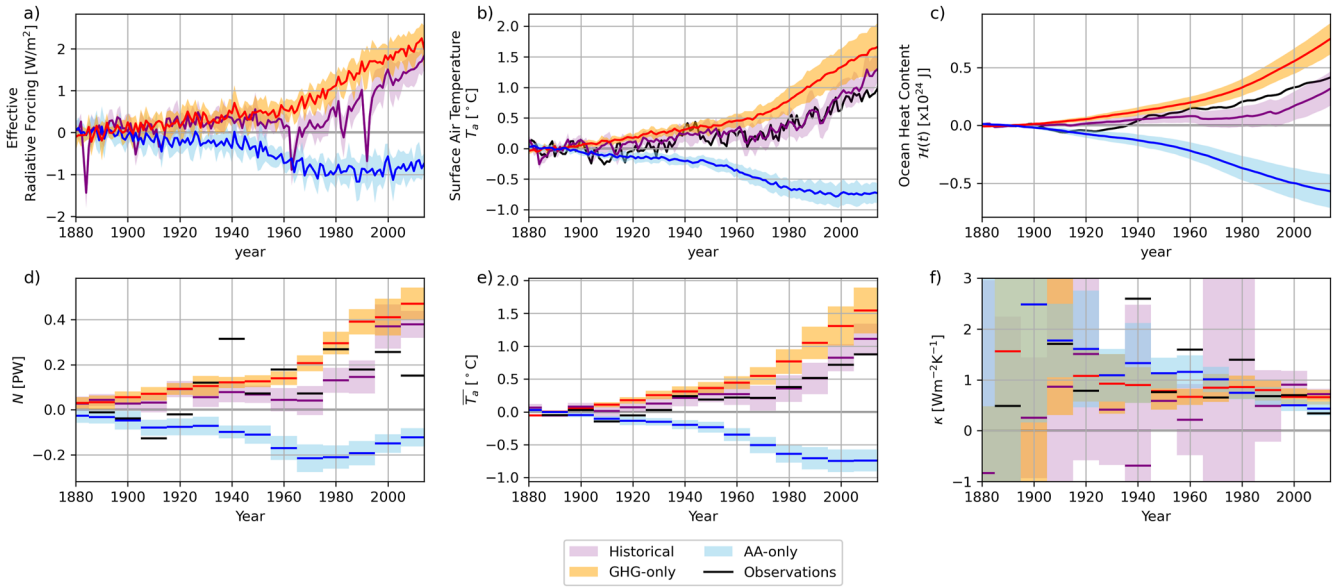

Figure 1. The (a) multi-model-mean effective radiative forcing (ERF), and multi-model-mean and observed, (b) and (e) global-mean surface air temperature T_a, (c) globally integrated ocean heat content $\mathcal{H}$, (d) globally integrated ocean heat content tendency, N, and (f) ocean heat uptake efficiency, κ. All quantities are shown separately for GHG-only (orange), AA-only (blue) and historical (all forcings, purple) simulations, as well as observations (black), and plotted relative to a 1880–1900 baseline. (a–c) are annual means, and (d–f) are decadal means. The standard deviation (shaded regions) illustrates the inter-model variance of the model ensemble-means analyzed. Note that the choice of y-axis limits in f) emphasizes later decades (which have lower inter-model variability), so some values of κ may be outside the bounds of the plot in some decades.

since the 1980s at sustained levels below pre-industrial, as shown in Figure 1a. This is largely mimicked by the surface air temperature field which has plateaued (Figure 1b). By contrast, although the rate of ocean cooling has slowed, ocean heat content has not stabilized (see Figure 1c). This could be due to the fact that the ocean equilibrates to changing surface forcing over long (decadal or greater) timescales, which have not yet been reached (Yang & Zhu, 2011). There may also be compensation in ocean heat content occurring between different oceanic regions, such that ocean warming in one region is offset by cooling elsewhere.

The historical ocean heat content (OHC), T_a, and ERF (purple lines in Figure 1a–1c) are a linear combination of the AA-only, GHG-only and natural forcings. Observational estimates of global surface air temperature (black lines in Figure 1b) closely align with the multi-model-mean from the historical simulation. However, the observed ocean heat content in Figure 1c is consistently larger than the envelope of CMIP6 estimates until after 2010. In addition, ocean heat content in observations grows quasi-linearly from 1960, while the CMIP6 historical simulations do not show significant ocean heat content growth until the 1990s.

Figures 1d–1f shows the ocean heat uptake, N, mean surface air temperature averaged over decadal time windows, $\overline{T_a}$, and ocean heat uptake efficiency, κ since 1880, which are related by Equation 2, in the GHG- and AA-only and historical simulations. Global ocean heat content tendency, N, has continued to grow since the 1980s in the GHG-only simulations (Figure 1d), reflecting the acceleration of ocean warming due to GHGs. Aerosol-driven ocean cooling, on the other hand, has begun to decelerate since the 1980s, matching the stabilization of ERF and mean surface air temperature during this time (Figure 1e), and N has tended to become less negative since the 1970s. The historical ocean heat uptake, N, (purple lines in Figure 1d) is again a linear combination of the AA-only, GHG-only and natural forcings. In this case, natural forcings have a meaningful impact on the rate of ocean heat uptake and historical N cannot be approximated as solely a linear combination of GHG-only and AA-only simulations. The observational N (black lines in Figure 1d) is higher than the multi-model-mean historical estimate after 1925 until the 1995–2004 decade. This may be due to a later ramp-up of ocean heat content in the CMIP6 historical simulation, or due to the fact that decadal variability has been largely averaged out in the CMIP6 multi-model-mean time series.

Ocean heat uptake efficiency κ has qualitatively different GHG-only, AA-only and historical responses. Prior to 1900, inter-model variability in κ is extremely large in all simulations due to the small signal in N and T_a. This

is especially true in the historical simulations, where a combination of a weak signal in N and T_a and higher inter-model variability leads to extremely uncertain estimates of κ until the 2000s and no discernible trend (see purple lines and shading in Figure 1f). In addition, the historical κ is not a linear combination of GHG-only, AA-only and natural forcings. This non-linearity is inevitable, given that historical N and $\overline{T_a}$ *are* linearly additive combinations of GHG-only, AA-only and natural forcings.

We calculate the uncertainty global ocean heat uptake efficiency as the standard deviation of the ensemble-averaged κ in each decadal window across the nine models assessed in this study. In the GHG-only simulations, κ has remained largely stable since the decades following 1945, averaging 0.75 $\pm$ 0.23 Wm^{-2} K^{-1}, as shown in Figure 1f. This range of κ lies within the average in observations over the same time period, 0.87 Wm^{-2} K^{-1}, and is consistent with previous estimates in strongly forced climate models and observations (Cael, 2022; Kuhlbrodt & Gregory, 2012; Winton et al., 2014). In AA-only simulations, κ has exhibited a sustained decline since the decades following 1945, from 1.13 $\pm$ 0.30 Wm^{-2} K^{-1} between 1945 and 1954 to 0.43 $\pm$ 0.14 Wm^{-2} K^{-1} between 2005 and 2014. The uncertainty in the change in κ between time windows is calculated as the standard deviation of the ensemble-averaged κ change (in %) between the windows of interest across the nine models assessed in this study. Overall, between 1975–1984 and 2005–2014, AA-only κ has declined by 43 $\pm$ 14%. The inter-model variability in this AA-only estimate has also approximately halved since the 1945 - 1954 decade, signaling that the ocean in most model members is exhibiting this drop in ocean heat uptake efficiency.

4.2. Layer-Wise Ocean Heat Uptake Efficiency

Our results show that, globally, both the rates of ocean cooling and the ocean heat uptake efficiency have dropped in response to aerosols (blue lines in Figures 1d and 1f). In order to distinguish *in which layers* this drop occurs, we calculate the layer-wise ocean heat uptake, following Equation 5 for temperature-percentiles and Equation 3 for depth layers in decadal time windows (see Figures 2a, 2b, 2e, and 2f). The layer-wise κ is then $N(p,t)/\left(\overline{T_a}A_T\right)$ in temperature-percentiles and $N(z,t)/\left(\overline{T_a}A_T\right)$ in depth (Figures 2c, 2d, 2g, and 2h), where A_T is the earth's surface area. Due to the different layer thickness in temperature-percentiles and depth, we cumulatively integrate from hot to cold or from top to bottom to enable a direct comparison.

The profiles of the multi-model-mean ocean heat content tendency in temperature-percentiles (or depth) are shown in Figures 2a and 2b for GHG-only and Figures 2e and 2f for AA-only simulations, from 1945 to 2014. The ocean heat content tendency in GHG-only simulations shows a warming across all temperature-percentile and depth classes (Figures 2a and 2b).

In an aerosol-forced ocean, prior to the 1980s, all water masses are cooling, and the $\overline{\Theta^p} > 5°C$ ($z < 2$ km) layer emerges as a key zone of ocean cooling (see Figures 2e and 2f). After the 1980s, the rate of cooling declines, and there is warming after the 1990s above 20°C ($z < 100$ m). Figure S1 (see Supporting Information S1) shows the CMIP6 multi-model-mean sea surface temperature, providing an indication of the regions that experience this recent warming. This suggests that soon after the plateauing of aerosol ERF, cooling of the upper ocean ceases in the warm tropics and subtropics, where equilibration to forcing is rapid, while continuing in colder polar and sub-polar regions and in the global mean. Cooling also continues in the deep ocean (i.e., $N < 0$) as the effect of previously growing negative ERF continues to spread downwards. The one-dimensional framework explored here does not enable us to distinguish the impact of inter-hemispheric and inter-basin transport on these results, something that is important given the distribution of and change in atmospheric aerosol concentrations is highly asymmetric (Li et al., 2023; Shi et al., 2023). In Section 5 we explore the potential impact of regional oceanic changes on our results based on prior research.

The layer-wise κ (shown in Figures 2c, 2d, 2g, and 2h) shows that under continuously increasing GHG forcing (Figures 2c and 2d) all layers make a fairly constant contribution to ocean heat uptake efficiency, which initially increases and later decreases slightly. In contrast, for aerosol forcing (Figures 2g and 2h) the contribution is fairly constant until the ERF plateaus but subsequently declines at all levels. Since 1995, the tropics and sub-tropics (above 20°C) have stopped cooling in response to surface cooling (see gray and mustard lines in Figure 2g). This is also seen in depth layers (Figure 2h) at depths above 100 m.

In order to quantify the inter-model variability between the nine climate models investigated in this study, we calculate the standard deviation across the ensemble-averaged layer-wise heat content tendency, air-sea heat fluxes and mixing (see Figures S2 and S3 in Supporting Information S1). The inter-model standard deviation in layer-wise heat content tendency (as shown by the slope in Figure S2 in Supporting Information S1) is large across

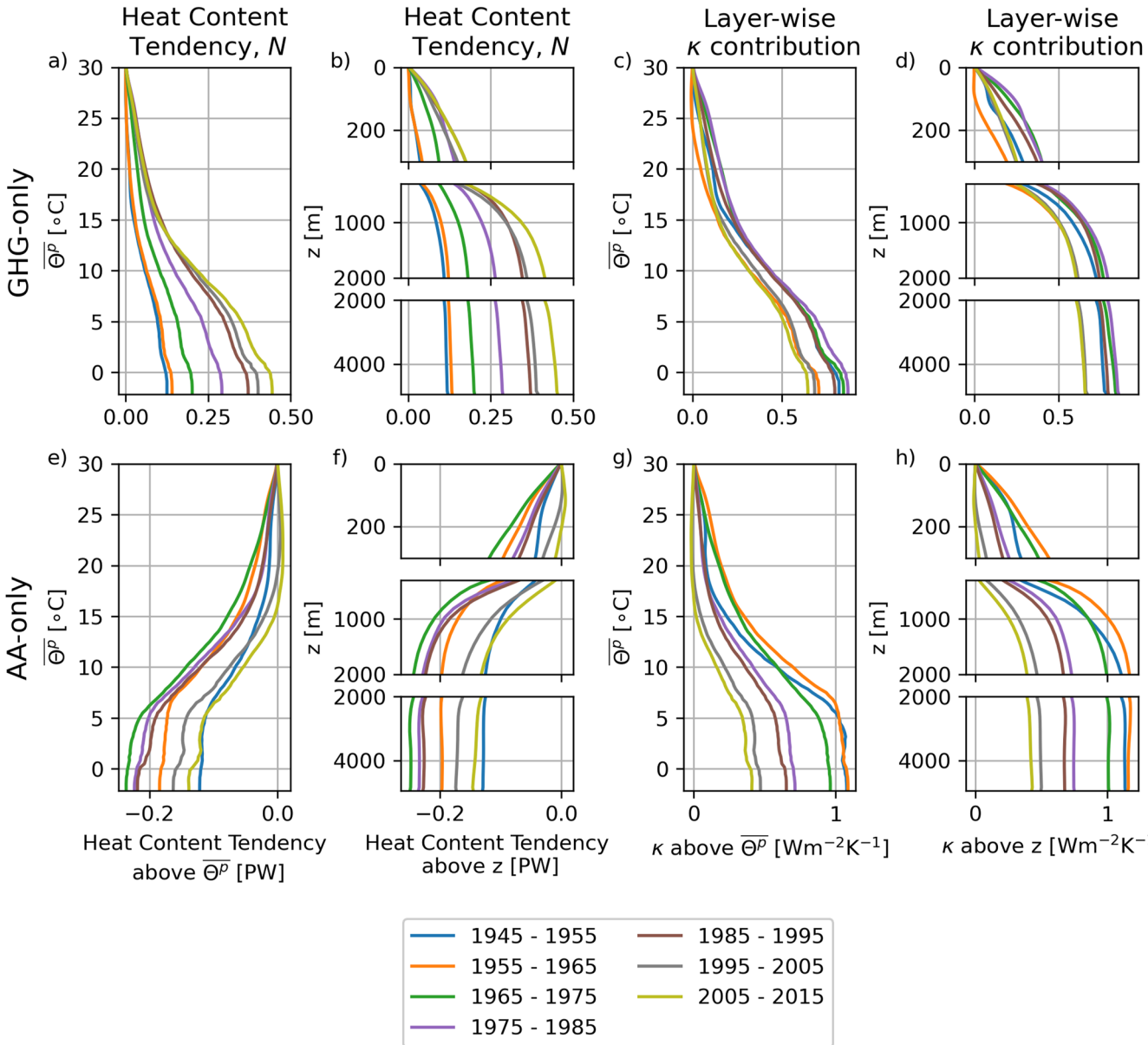

Figure 2. The multi-model-mean layer-wise ocean heat content tendency, N (a, b, e, and f), and ocean heat uptake efficiency contribution, κ (c, d, g, and h), in temperature-percentile (a, c, e, and g) and depth (b, d, f, and h) layers, across decadal windows from 1945–1954 to 2005–2014. The top row shows the GHG-only simulation results (a)–(d), while the bottom row shows the AA-only simulation results (e)–(h). To ease in visualization, we plot our temperature-percentile results in terms of the time-mean temperature of a given percentile surface, $\overline{\Theta^p}$.

all decades in the warmest (surface) layers, and is larger in depth layers compared with temperature-percentile layers. This implies that the recent tropical and sub-tropical warming signal in Figure 2e has lower inter-model variance than the surface warming in Figure 2f. In addition, the 15° C > $\overline{\Theta^p}$ > 5° C percentile layer represents another region of high inter-model heat content tendency variance. This layer outcrops in the sub-polar ocean (Figure S1 in Supporting Information S1), indicating that differences in model responses to surface fluxes may be large in these regions.

4.3. Layer-Wise Heat Content Budget

Air-sea heat fluxes can be diagnosed in temperature-percentiles from the DAMIP model outputs, and the diathermal mixing is calculated as the difference between the ocean heat content tendency and the change in surface heat

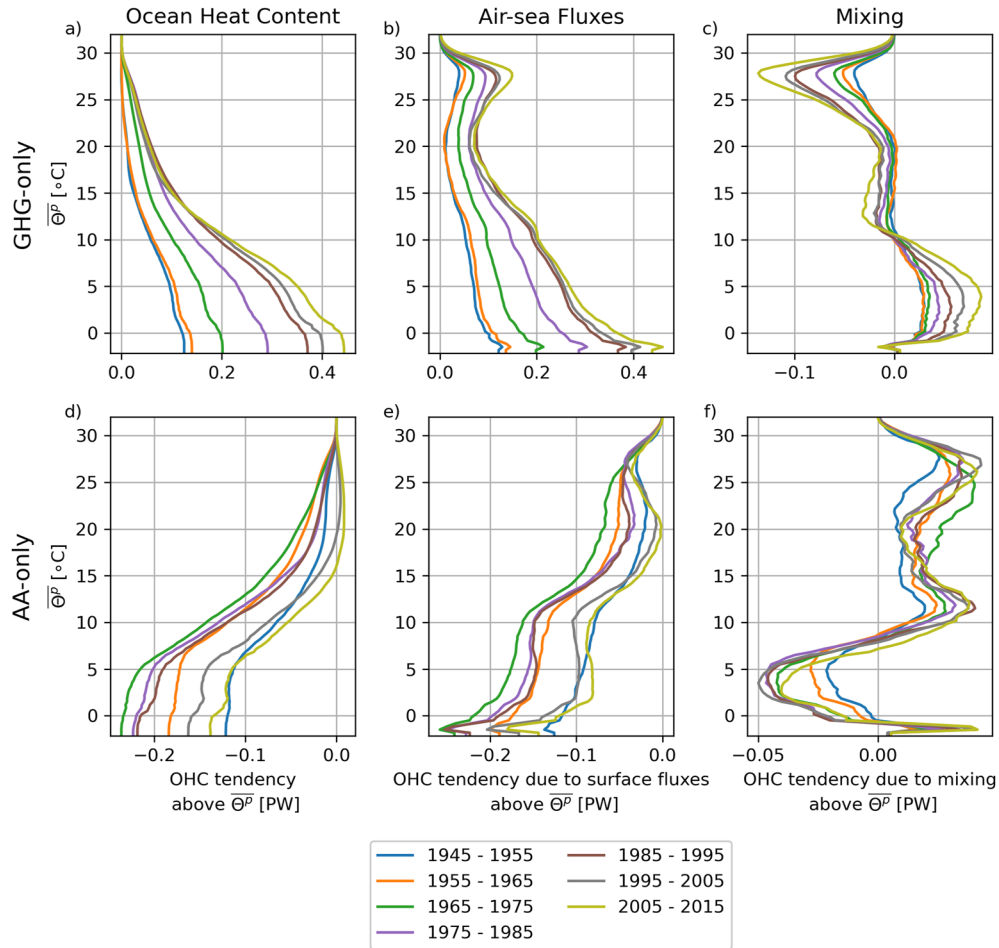

Figure 3. The multi-model-mean ocean heat content tendency (a and d), change in surface heat flux (b and e), and change in diathermal heat flux (c and f) in GHG-only (top row) and AA-only (bottom row) CMIP6 simulations, plotted in temperature-percentile space for decadal time windows from 1945 to 2014. Note that panels (a) and (d) are identical to panels (a) and (e) in Figure 2. To ease in visualization, we plot our results in terms of the time-mean temperature of a given percentile surface, $\overline{\Theta^p}$.

flux, given that there are no other terms in the heat budget. Thus, in Figures 3b and 3e, we present the ocean heat content tendency due to change in surface heat flux in the GHG-only and AA-only simulations, respectively, and in Figures 3c and 3f we show the tendency due to change in diathermal mixing in the GHG-only and AA-only simulations. Note that as the profiles of air-sea fluxes and mixing are cumulatively integrated from hot to cold, the *slope* of the profiles indicates whether surface heat fluxes or mixing are driving warming (negative slope) or cooling (positive slope).

In the GHG-only simulations, air-sea heat fluxes into the tropics ($\overline{\Theta^p} > 27$°C) and the sub-polar and polar regions ($\overline{\Theta^p} < 20$°C) drive ocean warming (see Figure S1 in Supporting Information S1 for the location of relevant temperature outcrops). In the sub-tropical gyres ($20 < \overline{\Theta^p} < 27$°C), on the other hand, air-sea fluxes drive ocean cooling. This tropical warming and sub-tropical cooling due to air-sea fluxes is consistent with a shift of surface warming toward the warmest temperature-percentiles at the ocean surface (the opposite trend is seen in the AA-only simulations). Generally, mixing tends to oppose the surface flux tendency, except in the polar and sub-polar regions and deep ocean ($5 < \overline{\Theta^p} < 10$°C), where mixing also drives ocean warming.

In the AA-only simulations, surface heat fluxes drive cooling across all temperature-percentile classes until the 1980s. Following the stabilization of the AA-only ERF in the 1980s, surface flux-driven cooling ceases in the tropics and sub-tropics (corresponding to temperatures above $\overline{\Theta^p} = 20$°C, see Figure S1 in Supporting Information S1). Air-sea fluxes into the sub-polar and polar regions (below $\overline{\Theta^p} = 20$°C), on the other hand, continue to

drive a cooling at a constant rate despite the ERF stabilization. This implies that AA-driven ocean cooling is sustained outside of the tropics and sub-tropics via air-sea fluxes.

Apart from the air-sea heat redistribution signal in the warmest temperature-percentiles (i.e., the bumps in Figures 3b and 3e in the $20 < \overline{\Theta^p} < 27$°C layers), there is a strong qualitative similarity between the total OHC tendency and the OHC tendency due to the change in air-sea heat flux. This similarity suggests that surface heat uptake is transported mostly isothermally in the interior, consistent with the isopycnal analysis of Saenko et al. (2021) and the isothermal analysis of Sohail et al. (2021) in historical CMIP6 simulations. As in the ocean heat uptake efficiency analysis in Section 4.2, the inter-model variability is large across all decades in the warmest temperature-percentiles for surface air-sea fluxes and mixing (see Figure S3 in Supporting Information S1).

Prior work from Exarchou et al. (2015) and Saenko et al. (2021) has shown that high-latitude heat uptake is driven by vertical mixing and neutral diffusion in strongly warming climate models under idealized future forcing scenarios. In order to explore whether this is true in the CMIP6 experiments assessed here, we analyze the 1995–2014 time period in a single climate model—ACCESS-CM2—for which detailed tendency budget terms are available. Our results corroborate this prior work, confirming that, in ACCESS-CM2, neutral diffusion (due to lateral eddies) and vertical mixing (likely due to convection) drive a significant amount of the ocean heat uptake in both the GHG-only and the AA-only simulations (see Figure S4 in Supporting Information S1). In addition, the mixing profiles in Figure 3 (which are inferred as the residual of ocean heat content tendency and surface fluxes) match the explicitly diagnosed mixing in ACCESS-CM2. Prior work has established that the representation of high latitude ocean processes in CMIP6 models is highly uncertain (Heuzé, 2020), and our results emphasize the importance of better representing polar and sub-polar processes in future climate projections of ocean heat content.

5. Discussion

In this work, we have explored the slowdown in ocean cooling due to aerosols since 1980. We use a set of single-forcing DAMIP simulations (comprising nine climate models and 48 ensemble members in total) forced by GHGs or AAs to investigate the time period, layers and processes driving this deceleration in aerosol-driven ocean cooling. We find that, despite aerosols' historic role in suppressing warming due to GHGs, since 1980 the ERF due to aerosols has stabilized and the ocean may have begun to equilibrate to this new climate state. Globally, the AA-only ocean has begun to cool less rapidly, and the global ocean heat uptake efficiency, which represents the response of ocean heat content to a degree of surface warming or cooling, has dropped by $43 \pm 14\%$ since the 1975–1984 decade. These decelerating rates of cooling and reduced heat uptake efficiency have been confined to the tropics and sub-tropics, driven by warmer-than-usual air-sea fluxes. In contrast, in the coldest layers (corresponding to the polar and sub-polar regions), air-sea heat fluxes have continued to sustain ocean cooling and drive up ocean heat uptake efficiency. Thus, the polar and sub-polar regions can still be cooled efficiently in response to aerosol forcing, offsetting the relatively efficient ocean warming due to greenhouse gasses.

The one-dimensional temperature-percentile framework used in this work does not enable an analysis of inter-hemispheric or inter-basin heat transport, or of the regional mechanisms which drive the ocean heat content change. Boland et al. (2023) found the strongest cooling response to aerosol forcing occurs in the North Atlantic and Southern Ocean (which aligns roughly with $\Theta < 20$°C at the surface; see Figure S1 in Supporting Information S1 for a map of sea surface temperatures in the CMIP6 models). Li et al. (2023) suggested inter-basin circulation may be just as influential as ocean heat uptake patterns in modifying regional ocean heat tendencies, and Kang et al. (2021) identified a recent zonal shift in aerosol forcing between the North Atlantic and North Pacific. Processes such as these affect the relationship between sea surface temperature and ocean heat uptake, and therefore could cause the aerosol-driven ocean heat uptake efficiency to change. Thus, they offer alternatives to our hypothesis, that its decline is due to stabilization of aerosol ERF. Future research may determine the specific regional mechanisms that drive this change.

The temperature-percentile framework shows promise for use with other strongly forced model simulations. The temperature-percentile framework enables more direct comparisons between models and observations which may have different mean states but have a similar volumetric temperature distribution. It also allows for large multi-model analyses by simplifying the heat budget and reducing the impact of drifting isotherms on the analysis of strongly forced simulations, such as in future scenarios. New two-dimensional percentile methods, such as the

partitioning method presented in Sohail et al. (2023), show some promise in preserving spatial details, and may be used to extend this analysis in the future.

Data Availability Statement

The CMIP6 data used in this work is publicly available, and the full list of CMIP6 models used as well as their corresponding ensemble members is provided in Table S1 in Supporting Information S1. Effective Radiative Forcing data and code for calculations are sourced directly from Smith (2021). NASA GISSTEMPv4 data for global surface air temperature is sourced from GISS (2023). The code and files necessary to completely reproduce this analysis are provided at Sohail (2023).

Acknowledgments
We acknowledge the World Climate Research Program, the CMIP6 climate modeling groups, the Earth System Grid Federation (ESGF), and the funding agencies supporting CMIP6 and ESGF. Modeling and analysis were undertaken with National Computational Infrastructure (NCI) facilities, supported by the Australian Government. This work is supported by the Australian Research Council (ARC) Center of Excellence for Climate Extremes, the Australian Center for Excellence in Antarctic Science (SR200100008), and the ARC Discovery Project scheme (DP190101173). Open access publishing facilitated by University of New South Wales, as part of the Wiley - University of New South Wales agreement via the Council of Australian University Librarians.

References

Bi, D., Dix, M., Marsland, S., O'Farrell, S., Sullivan, A., Bodman, R., et al. (2020). Configuration and spin-up of ACCESS-CM2, the new generation Australian community climate and Earth system simulator coupled model. *Journal of Southern Hemisphere Earth Systems Science*, *70*(1), 225–251. https://doi.org/10.1071/es19040

Bilbao, R. A. F., Gregory, J. M., Bouttes, N., Palmer, M. D., & Stott, P. (2019). Attribution of ocean temperature change to anthropogenic and natural forcings using the temporal, vertical and geographical structure. *Climate Dynamics*, *53*(9–10), 5389–5413. https://doi.org/10.1007/s00382-019-04910-1

Boland, E. J. D., Dittus, A. J., Jones, D. C., Josey, S. A., & Sinha, B. (2023). Ocean heat content responses to changing anthropogenic aerosol forcing strength: Regional and multi-decadal variability. *Journal of Geophysical Research: Oceans*, *128*(7), e2022JC018725. https://doi.org/10.1029/2022jc018725

Cael, B. B. (2022). Ocean heat uptake efficiency increase since 1970. *Geophysical Research Letters*, *49*(19), e2022GL100215. https://doi.org/10.1029/2022gl100215

Delworth, T. L., Ramaswamy, V., & Stenchikov, G. L. (2005). The impact of aerosols on simulated ocean temperature and heat content in the 20th century. *Geophysical Research Letters*, *32*(24), L24709. https://doi.org/10.1029/2005gl024457

Exarchou, E., Kuhlbrodt, T., Gregory, J. M., & Smith, R. S. (2015). Ocean heat uptake processes: A model Intercomparison. *Journal of Climate*, *28*(2), 887–908. https://doi.org/10.1175/jcli-d-14-00235.1

Eyring, V., Bony, S., Meehl, G. A., Senior, C. A., Stevens, B., Stouffer, R. J., & Taylor, K. E. (2016). Overview of the coupled model intercomparison project phase 6 (CMIP6) experimental design and organization. *Geoscientific Model Development*, *9*(5), 1937–1958. https://doi.org/10.5194/gmd-9-1937-2016

Gillett, N. P., Shiogama, H., Funke, B., Hegerl, G., Knutti, R., Matthes, K., et al. (2016). The detection and attribution model intercomparison project (DAMIP v1.0) contribution to CMIP6. *Geoscientific Model Development*, *9*(10), 3685–3697. https://doi.org/10.5194/gmd-9-3685-2016

GISS. (2023). GISTEMP team, 2023: GISS surface temperature analysis (GISTEMP), version 4 [Dataset]. Retrieved from https://data.giss.nasa.gov/gistemp/

Gleckler, P. J., Wigley, T. M. L., Santer, B. D., Gregory, J. M., AchutaRao, K., & Taylor, K. E. (2006). Krakatoa's signature persists in the ocean. *Nature*, *439*(7077), 675. https://doi.org/10.1038/439675a

Heuzé, C. (2020). Antarctic bottom water and North Atlantic deep water in CMIP6 models. *Ocean Science*, *17*(1), 59–90. https://doi.org/10.5194/os-17-59-2021

Holmes, R. M., Sohail, T., & Zika, J. D. (2022). Adiabatic and diabatic signatures of ocean temperature variability. *Journal of Climate*, *35*(5), 1459–1477. https://doi.org/10.1175/jcli-d-21-0695.1

Irving, D. B., Hobbs, W., Church, J. A., & Zika, J. D. (2020). A mass and energy conservation analysis of drift in the CMIP6 ensemble. *Journal of Climate*, *34*(8), 3157–3170. https://doi.org/10.1175/jcli-d-20-0281.1

Irving, D. B., Wijffels, S., & Church, J. A. (2019). Anthropogenic aerosols, greenhouse gases, and the uptake, transport, and storage of excess heat in the climate system. *Geophysical Research Letters*, *46*(9), 4894–4903. https://doi.org/10.1029/2019gl082015

Kang, S. M., Xie, S.-P., Deser, C., & Xiang, B. (2021). Zonal mean and shift modes of historical climate response to evolving aerosol distribution. *Science Bulletin*, *66*(23), 2405–2411. https://doi.org/10.1016/j.scib.2021.07.013

Kuhlbrodt, T., & Gregory, J. M. (2012). Ocean heat uptake and its consequences for the magnitude of sea level rise and climate change. *Geophysical Research Letters*, *39*(18), L18608. https://doi.org/10.1029/2012gl052952

Lenssen, N., Schmidt, G., Hansen, J., Menne, M., Persin, A., Ruedy, R., & Zyss, D. (2019). Improvements in the GISTEMP uncertainty model. *Journal of Geophysical Research: Atmospheres*, *124*(12), 6307–6326. https://doi.org/10.1029/2018jd029522

Li, S., Liu, W., Allen, R. J., Shi, J.-R., & Li, L. (2023). Ocean heat uptake and interbasin redistribution driven by anthropogenic aerosols and greenhouse gases. *Nature Geoscience*, *16*(8), 695–703. https://doi.org/10.1038/s41561-023-01219-x

Lyu, K., Zhang, X., & Church, J. A. (2021). Projected ocean warming constrained by the ocean observational record. *Nature Climate Change*, *11*(10), 1–6. https://doi.org/10.1038/s41558-021-01151-1

Palmer, M. D., & McNeall, D. J. (2014). Internal variability of Earth's energy budget simulated by CMIP5 climate models. *Environmental Research Letters*, *9*(3), 034016. https://doi.org/10.1088/1748-9326/9/3/034016

Ramanathan, V., Crutzen, P. J., Kiehl, J. T., & Rosenfeld, D. (2001). Aerosols, climate, and the hydrological cycle. *Science*, *294*(5549), 2119–2124. https://doi.org/10.1126/science.1064034

Raper, S. C. B., Gregory, J. M., & Stouffer, R. J. (2002). The role of climate sensitivity and ocean heat uptake on AOGCM transient temperature response. *Journal of Climate*, *15*(1), 124–130. https://doi.org/10.1175/1520-0442(2002)015⟨0124:trocsa⟩2.0.co;2

Saenko, O. A., Gregory, J. M., Griffies, S. M., Couldrey, M. P., & Dias, F. B. (2021). Contribution of ocean physics and dynamics at different scales to heat uptake in low-resolution AOGCMs. *Journal of Climate*, *34*(6), 2017–2035. https://doi.org/10.1175/jcli-d-20-0652.1

Schuckmann, K. V., Cheng, L., Palmer, M. D., Hansen, J., Tassone, C., Aich, V., et al. (2020). Heat stored in the Earth system: Where does the energy go? *Earth System Science Data*, *12*(3), 2013–2041. https://doi.org/10.5194/essd-12-2013-2020

Shi, J., Kwon, Y., & Wijffels, S. E. (2023). Subsurface ocean temperature responses to the anthropogenic aerosol forcing in the North Pacific. *Geophysical Research Letters*, *50*(2), e2022GL101035. https://doi.org/10.1029/2022gl101035

Silvy, Y., Guilyardi, E., Sallée, J.-B., & Durack, P. J. (2020). Human-induced changes to the global ocean water masses and their time of emergence. *Nature Climate Change*, *10*(11), 1–7. https://doi.org/10.1038/s41558-020-0878-x

Smith, C. J. (2021). chrisroadmap/cmip5-cmip6-forcing: Suppressed late-20th Century warming in CMIP6 models explained by forcing and feedbacks [Dataset]. Zenodo. https://doi.org/10.5281/zenodo.5421581

Smith, C. J., & Forster, P. M. (2021). Suppressed late-20th century warming in CMIP6 models explained by forcing and feedbacks. *Geophysical Research Letters*, *48*(19), e2021GL094948. https://doi.org/10.1029/2021gl094948

Smith, C. J., Harris, G. R., Palmer, M. D., Bellouin, N., Collins, W., Myhre, G., et al. (2021). Energy budget constraints on the time history of aerosol forcing and climate sensitivity. *Journal of Geophysical Research: Atmospheres*, *126*(13), e2020JD033622. https://doi.org/10.1029/2020jd033622

Sohail, T. (2023). Ocean heat content change in DAMIP simulations [Software]. Zenodo. https://doi.org/10.5281/zenodo.10121522

Sohail, T., Holmes, R. M., & Zika, J. D. (2023). Watermass co-ordinates isolate the historical ocean warming signal. *Journal of Climate*, *36*(9), 1–40. https://doi.org/10.1175/jcli-d-22-0363.1

Sohail, T., Irving, D. B., Zika, J. D., Holmes, R. M., & Church, J. A. (2021). Fifty year trends in global ocean heat content traced to surface heat fluxes in the sub-polar ocean. *Geophysical Research Letters*, *48*(e2020GL091439), 1–13. https://doi.org/10.1029/2020gl091439

Sohail, T., Zika, J. D., Irving, D. B., & Church, J. A. (2022). Observed poleward freshwater transport since 1970. *Nature*, *602*(7898), 617–622. https://doi.org/10.1038/s41586-021-04370-w

Winton, M., Anderson, W. G., Delworth, T. L., Griffies, S. M., Hurlin, W. J., & Rosati, A. (2014). Has coarse ocean resolution biased simulations of transient climate sensitivity? *Geophysical Research Letters*, *41*(23), 8522–8529. https://doi.org/10.1002/2014gl061523

Yang, H., & Zhu, J. (2011). Equilibrium thermal response timescale of global oceans. *Geophysical Research Letters*, *38*(14), L14711. https://doi.org/10.1029/2011gl048076

Zanna, L., Khatiwala, S., Gregory, J. M., Ison, J., & Heimbach, P. (2019). Global reconstruction of historical ocean heat storage and transport. *Proceedings of the National Academy of Sciences of the United States of America*, *116*(4), 1126–1131. (Zanna also contributes OH tendency to redistribution, unable to specify the processes that may be contributing to differences in storage.). https://doi.org/10.1073/pnas.1808838115